

## Probing neutron star structure via $f$ -mode oscillations and damping in dynamical spacetime models

Shawn G. Rosofsky,<sup>1,2</sup> Roman Gold,<sup>3,4,5</sup> Cecilia Chirenti,<sup>6</sup> E. A. Huerta,<sup>1,7</sup> and M. Coleman Miller<sup>8</sup>

<sup>1</sup>*NCSA, University of Illinois at Urbana-Champaign, Urbana, Illinois 61801, USA*

<sup>2</sup>*Department of Physics, University of Illinois at Urbana-Champaign, Urbana, Illinois 61801, USA*

<sup>3</sup>*Institut für Theoretische Physik, Johann Wolfgang Goethe-Universität,  
Max-von-Laue-Straße 1, 60438 Frankfurt, Germany*

<sup>4</sup>*Department of Physics and Joint Space-Science Institute, University of Maryland,  
College Park, Maryland 20742-2421, USA*

<sup>5</sup>*Perimeter Institute for Theoretical Physics, 31 Caroline Street North, Waterloo,  
Ontario N2L 2Y5, Canada*

<sup>6</sup>*Center for Mathematics, Computation and Cognition, UFABC, Santo André-São Paulo,  
09210-580, Brazil*

<sup>7</sup>*Department of Astronomy, University of Illinois at Urbana-Champaign, Urbana, Illinois 61801, USA*

<sup>8</sup>*Department of Astronomy and Joint Space-Science Institute, University of Maryland,  
College Park, Maryland 20742-2421, USA*



(Received 14 December 2018; published 15 April 2019)

Gravitational wave and electromagnetic observations can provide new insights into the nature of matter at supranuclear densities inside neutron stars. Improvements in electromagnetic and gravitational wave sensing instruments continue to enhance the accuracy with which they can measure the masses, radii, and tidal deformability of neutron stars. These better measurements place tighter constraints on the equation of state of cold matter above nuclear density. In this article, we discuss a complementary approach to get insights into the structure of neutron stars by providing a model prediction for nonlinear fundamental eigenmodes ( $f$  modes) and their decay over time, which are thought to be induced by time-dependent tides in neutron star binaries. Building on pioneering studies that relate the properties of  $f$  modes to the structure of neutron stars, we systematically study this link in the nonperturbative regime using models that utilize numerical relativity. Using a suite of fully relativistic numerical relativity simulations of oscillating Tolman-Oppenheimer-Volkoff stars, we establish blueprints for the numerical accuracy needed to accurately compute the frequency and damping times of  $f$ -mode oscillations, which we expect to be a good guide for the requirements in the binary case. We show that the resulting  $f$ -mode frequencies match established results from linear perturbation theory, but the damping times within numerical errors depart from linear predictions. This work lays the foundation for upcoming studies aimed at a comparison of theoretical models of  $f$ -mode signatures in gravitational waves, and their uncertainties with actual gravitational wave data, searching for neutron star binaries on highly eccentric orbits, and probing neutron star structure at high densities.

DOI: [10.1103/PhysRevD.99.084024](https://doi.org/10.1103/PhysRevD.99.084024)

### I. INTRODUCTION

Neutron stars [1] present unique opportunities to study the nature of matter at supranuclear densities at relatively low temperatures, and in the presence of extreme gravitational interactions. Given the diverse scenarios that have been invoked to describe the properties of cold, dense matter in the cores of neutron stars (nucleons, hyperons, or free quarks) [2–5], it is essential to confront these theories with observations in the gravitational or electromagnetic spectrum, or a combination of them through multimessenger astrophysics discovery campaigns [6,7]. These studies will constrain the space of permissible models

and hopefully, gain a better understanding of the physics at supranuclear densities. Electromagnetic observations of the pulsars PSR J1614-2230 [8] and PSR 0348 + 0432 [9], which are consistent with neutron stars with masses  $M \sim 2 M_{\odot}$ , have already significantly reduced the existing number of astrophysically viable equations of state (EOS),  $P(\epsilon)$ , i.e., the relation between the pressure  $P$  and the total energy density  $\epsilon$ . In [10] an upper limit for the neutron star maximum mass of  $M = 2.16 M_{\odot}$  was derived based on GW170817 and basic arguments on kilonovas. A consistent limit was derived from different considerations [11] based on previous arguments about the nature of short gamma-ray bursts [12–14].

X-ray observations of the pulse profiles generated by hot spots on moderately spinning neutron stars with the ongoing NICER [15] and future enhanced X-ray Timing and Polarimetry (eXTP) [16] missions may enable measurements of the neutron star radii at the 5% level [17], improving existing measurements that are dominated by systematic errors [18,19]. This precision can be achieved through long exposure times using NICER, or using the polarimetry capabilities of eXTP.

LIGO [20,21] and Virgo [22] gravitational wave (GW) observations of the neutron star merger GW170817 [6,7,23] imply that the two neutron stars had radii  $R_{\{1,2\}} = 11.9_{-1.4}^{+1.4}$  km. Moreover, these measurements constrain the dimensionless tidal deformability  $\tilde{\Lambda} \lesssim 800$  [6]. Furthermore, following [24,25], one can express the logarithm of the adiabatic index of the EOS  $\Gamma(P, \gamma_i)$  as a polynomial of the pressure  $P$  ( $\gamma_i$  are the free EOS parameters). In this so-called spectral parametrization, the adiabatic index is used to compute the energy  $\epsilon(P; \gamma_i)$  and the rest-mass density  $\rho(P; \gamma_i)$ . Thereafter, these two latter quantities are inverted to give the EOS. Finally, this parametrization is connected to the SLy EOS [26] below half of the nuclear density. Using this approach, and imposing a number of constraints to ensure causality, internal, and observational consistency, the study presented in [27] sampled directly the EOS parameter space, and inferred that the pressure at twice the nuclear saturation density of the GW170817 system is measured to be  $P(2\epsilon_{\text{nuc}}) = 3.5_{-1.7}^{+2.7} \times 10^{34}$  dyn cm<sup>-2</sup> quantified at the 90% confidence level.

As a reference point, terrestrial laboratories can only test and constrain cold EOSs at densities near or below saturation density of nuclei  $\epsilon_{\text{nuc}}$ . GW observations enable these measurements because the waveform models used to analyze LIGO and Virgo data encode information about the static and dynamic tides that determine the dynamical evolution of the system, driving it to merger faster than a system of two point masses [28–31].

GW and electromagnetic observations will continue to provide new and detailed information about the nature of neutron star matter. GW observations will shed light on the masses and tidal deformability of neutron stars, while electromagnetic observations will enable accurate measurements of their mass and radius [15] and may even be informative for studies of stellar structure in the context of non-GR spacetimes [32].

Even though multimessenger observations will provide new and detailed information about the properties of neutron stars, they are likely to leave open questions, especially in light of potential emission-model dependence, which calls for independent and complementary measurements. In this article, we will focus on a different observational scenario to obtain this information from direct observations of the stars, namely, the measurement of fundamental eigenmodes ( $f$  modes) of the individual

stars, which can be caused by tidal effects, and for which pressure is the restoring force.

Proposed scenarios for the generation of  $f$  modes in neutron stars include neutron star binaries or neutron star–black hole systems in highly eccentric orbits [33–39], i.e., binary separations comparable to the radii of the binary components, such that violent changes in the tidal field can perturb the stars without necessarily causing an immediate collision [40–45]. These close interactions will induce  $f$ -mode oscillations in cold, slowly rotating neutron stars, thereby simplifying the analysis and modeling of  $f$  modes as compared to the differentially rotating scenario [40] or shock heated matter in hypermassive neutron stars [46–49].

Extracting physics encoded in the  $f$  modes from observational data involves an accurate model prediction [50,51], and measurement of their frequencies  $\omega$  and damping times  $\tau$ . Seminal studies have established that these two observables are related to the average density and compactness [52–54]. In [55,56] universal relations using the effective compactness  $\eta = (M/I^3)^{1/2}$  with mass  $M$  and moment of inertia  $I$  were discovered, and were tested in [57].

In principle, once  $\omega$  and  $\tau$  are extracted from GW observations, it may be possible to infer  $M$  and  $I$ . Furthermore, the amplitude of the  $f$  mode depends on the orbital energy deposited in the mode, and this can be used to measure the Love number  $\lambda$  and the rotationally induced quadrupole  $Q$  through  $I$ -Love- $Q$  relations [58–61].

In this article, we carry out detailed analyses to quantify the required accuracy in numerical relativity simulations to extract the  $f$ -mode oscillations and damping times. To do this, we simulate oscillating neutron stars using the open source EINSTEIN TOOLKIT numerical relativity software, and compare these results to linear perturbation theory (where appropriate) similar in setup and spirit to [62], but with a different focus. In addition to perturbations in the linear regime we also explore perturbation amplitudes more akin to those seen in highly eccentric neutron star binary tidal interactions. This work lays the foundation for future numerical relativity simulations of highly eccentric neutron star mergers (see [63] for a state-of-the-art library) with the aim of accurately extracting  $f$ -mode oscillation damping times and frequencies as well as a systematic investigation for a variety of equations of state and the effect of model uncertainties on parameter estimation. A successful detection and accurate parameter estimation from eccentric neutron star binaries would provide a wealth of information on astrophysical evolution scenarios [64].

This article is organized as follows: Sec. II outlines the approach we have followed to couple Einstein’s field equations with a relativistic perfect fluid. We describe the construction of initial data to excite  $f$ -mode oscillations in Tolman-Oppenheimer-Volkoff (TOV) stars, and the extraction of the corresponding GWs. In Sec. III, we show that the numerical formalism introduced in this study exhibits the necessary convergence to accurately compute

the frequency and damping time of  $f$ -mode oscillations. We also demonstrate that our simulations reproduce the expected results from linear perturbation theory in the appropriate limit. We summarize our findings and future directions of work in Sec. IV.

## II. METHODS

We evolve the spacetime by solving the Einstein field equations using the tools of numerical relativity

$$R_{\mu\nu} - \frac{1}{2}Rg_{\mu\nu} = 8\pi T_{\mu\nu}. \quad (1)$$

We express the four-dimensional metric  $g_{\mu\nu}$  in the standard 3 + 1 split of spacetime [65–70] as

$$ds^2 = -\alpha^2 dt^2 + \gamma_{ij}(dx^i + \beta^i dt)(dx^j + \beta^j dt) \quad (2)$$

with the spatial metric  $\gamma_{ij}$  induced on each hypersurface of the spacetime foliation, the lapse  $\alpha$ , shift  $\beta^i$ , and the hypersurface unit normal vector

$$n^\mu = \left( \alpha^{-1}, -\frac{\beta^i}{\alpha} \right). \quad (3)$$

Projecting the Einstein equations onto the hypersurface and along  $n^\mu$  yields a set of constraint and evolution equations that together with suitable initial data form our initial value problem.

### A. Spacetime evolution

There are infinitely many formulations of the Einstein equations that are equivalent in the continuum limit of infinite spatial and temporal resolution, but that have distinct principal parts and hyperbolicity properties, and hence behave differently at finite resolution. In this study we primarily employed the Baumgarte-Shapiro-Shibata-Nakamura (BSSN) formalism [71,72], though the CCZ4 formalism [73] was also used for some results. For the cases in this work in which the conformal and covariant Z4 (CCZ4) formulation was used, we set the damping coefficients  $\kappa_1 = 0.02$  and  $\kappa_2 = 0$ .

The evolution of the gauge conditions, i.e., lapse and shift, is governed by standard 1 + log slicing condition and a Gamma driver (see e.g., [67,74]).

We are making use of the publicly available MCLACHLAN code [75] which implements the above evolution equations with fourth order central finite differences and is part of the EINSTEIN TOOLKIT [76].

The nonlinear stability of smoothness properties of the spacetime evolution is enhanced by adding an artificial Kreiss-Oliger dissipation [77] to the spacetime variables.

### B. General relativistic hydrodynamics

The neutron stars are modeled by a relativistic perfect fluid

$$T_{\mu\nu} = \rho h u_\mu u_\nu + p g_{\mu\nu} \quad (4)$$

where  $u^\mu$  is the 4-velocity,  $\rho$  is the rest mass,  $h$  is the specific enthalpy, and  $p$  is the pressure of the fluid.

The standard relativistic hydrodynamic equations are the local conservation law for the energy-momentum tensor

$$\nabla_\mu T^{\mu\nu} = 0, \quad (5)$$

and the conservation of rest mass

$$\nabla_\mu(\rho u^\mu) = 0. \quad (6)$$

Both equations together with the spacetime metric  $g_{\mu\nu}$  represent the equations of motion of the fluid, which are closed by a suitable EOS with the general form  $p = p(\rho, T, Y_e)$  where  $T$  is the temperature and  $Y_e$  the so-called electron fraction (low  $Y_e$  indicates neutron-rich material). In this pilot study we restrict ourselves to polytropes, but in the future we intend to investigate more realistic equations of state.

These equations can be cast into conservative form, which is also known as the ‘‘Valencia formulation’’ [78]

$$\partial_t \mathbf{U} + \partial_i \mathbf{F}^i = \mathbf{S} \quad (7)$$

where the conserved variables  $\mathbf{U}$  are defined by

$$\frac{\mathbf{U}}{\sqrt{\gamma}} = \begin{pmatrix} D \\ S_j \\ \tau \end{pmatrix} = \begin{pmatrix} \rho W \\ \rho h W^2 v_j \\ \rho h W^2 - p - \rho W \end{pmatrix} \quad (8)$$

and the fluxes as well as the sources are given by

$$\frac{\mathbf{F}^i}{\sqrt{\gamma}} = \begin{pmatrix} D(\alpha v^i - \beta^i) \\ \alpha \tilde{S}_j^i - \beta S_j \\ \alpha(S^i - Dv^i) - \tau \beta^i \end{pmatrix}. \quad (9)$$

These conservation equations are implemented in the EINSTEIN TOOLKIT’s GRHydro code [79], which uses high-resolution shock-capturing methods.

We employ a fourth order Runge-Kutta method to advance in time, either the weighted essentially non-oscillatory (WENO) or piecewise parabolic method (PPM) reconstruction method, second order flux evaluations, and either the Harten-Lax-van Leer-Einfeldt (HLLC) or Marquina Riemann solver. We set the Courant factor to 0.4.

Since we are not able to accurately track regions that transition from the fluid to the vacuum regime, all simulations have an artificial low-density background atmosphere which is evolved freely. For all simulations presented in this study we choose an atmosphere value of  $\rho_{\text{atm}} = 10^{-10} \text{ M}^{-2} \approx 6.2 \times 10^7 \text{ g/cm}^3$  or  $\rho_{\text{atm}} = 10^{-14} \text{ M}^{-2} \approx 6.2 \times 10^3 \text{ g/cm}^3$ .

### C. Initial data

We use a perturbed TOV solution as initial data. The matter perturbation is implemented by adding the (2,2) pressure eigenfunction of an incompressible Newtonian star in the Cowling approximation [80]. This form of the perturbation is smooth and provides a well-controlled framework to quantify numerical accuracy.

Specifically, the initial data were created with the EINSTEIN TOOLKIT's TOVSOLVER thorn. Then, we added a pressure perturbation to excite  $f$ -mode oscillations using an expression derived in the Cowling approximation. The perturbation was given by

$$\delta P = \alpha \rho \left( \frac{r}{R} \right)^2 Y_{22} \quad (10)$$

where  $\delta P$  is the perturbed pressure,  $\alpha$  is the amplitude of the perturbation,  $\rho$  is density,  $r$  is radial distance from the center of the star,  $R$  is the radius of the star, and  $Y_{22}$  is the  $l = 2$   $m = 2$  spherical harmonic. A plot of the density distribution resulting from this perturbation can be seen in Fig. 1.

### D. Equation of state

We adopt a polytropic equation of state

$$P = K \rho^\Gamma \quad (11)$$

where  $\Gamma$  is the adiabatic index and  $K$  is the constant of proportionality. For this work, we examined a polytrope with  $\Gamma = 2$  and  $K = 100$  which is a common choice in the

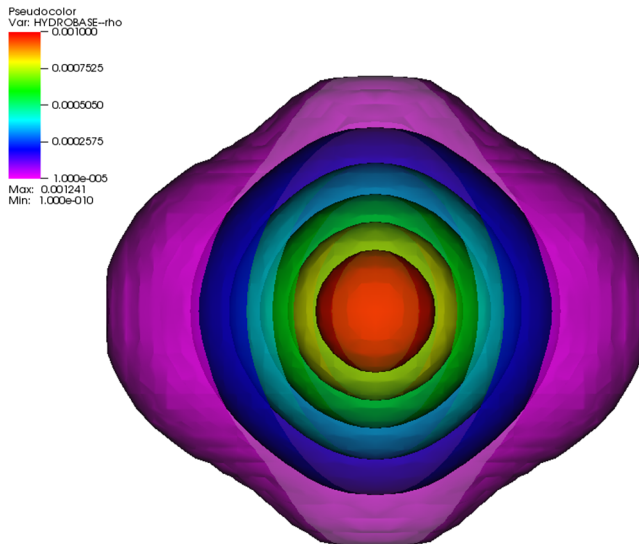


FIG. 1. Plot of density contours  $\rho$  (in code units) of a strongly perturbed TOV solution. The star was excited using a pressure perturbation that was derived in the Cowling approximation to induce  $f$ -mode oscillations. The perturbation amplitude is chosen as  $\alpha = 0.141$  for the star shown in the figure.

literature. We leave to future work the expansion of the methods applied in this paper to other EOSs.

### E. Grid setup

The numerical grid is managed by the mesh refinement CARPET [81] driver for CACTUS [82].

It implements a nonuniform grid via a nested set of movable boxes (box-in-box) together with a hierarchical (Berger-Oliger-style) time stepping. In these simulations we employ four refinement levels where each additional level doubles the resolution of the enclosing one. On the finest grid, which is separately centered around each neutron star, the resolution in each dimension is  $\Delta x = 0.0625 \text{ M} \approx 93.75 \text{ m}$  for the highest resolution. The physical domain extends to  $128 \text{ M} \approx 192 \text{ km}$ .

### F. Gravitational waves

The gravitational wave strain is extracted using the standard Newman-Penrose formalism [83], in which a particular contraction of the Weyl tensor with a suitably chosen null tetrad yields a gauge-invariant quantity  $\psi_4$  that encodes the outgoing gravitational radiation [84]. Specifically,  $\psi_4$  is related to the second time derivative of the two strain polarizations  $\ddot{h}_{+,x}$  by

$$\ddot{h}_+ - i\ddot{h}_x = \psi_4 = \sum_{\ell=2}^{\infty} \sum_{m=-\ell}^{\ell} \psi_4^{\ell m} {}_{-2}Y_{\ell m}(\theta, \varphi), \quad (12)$$

where we also introduced the multipole expansion of  $\psi_4$  in spin-weighted spherical harmonics [85] of spin weight  $s = -2$ .

### G. Models

We employed various models in which we altered simulation parameters such as perturbation amplitude, the spacetime formalism, etc. We present and label these models in Table I. All models used a  $1.4 M_\odot$  TOV star which had a central density of  $0.00128 \text{ M}^{-2}$  and the EOS described in Sec. IID.

TABLE I. This table lists all of the models in the first column and the important quantities that changed between models. These quantities were the spacetime formalism, the atmospheric density  $\rho_{\text{atm}}$ , the perturbation amplitude  $\alpha$ , the Riemann solver, and the reconstruction method.

Model	Formalism	$\rho_{\text{atm}} (\text{M}^{-2})$	$\alpha$	Riemann	Recon.
PPM big $\alpha$	BSSN	$10^{-10}$	0.141	Marquina	PPM
PPM big $\rho_{\text{atm}}$	BSSN	$10^{-10}$	0.0141	Marquina	PPM
PPM CCZ4	CCZ4	$10^{-10}$	0.0141	Marquina	PPM
PPM	BSSN	$10^{-14}$	0.0141	Marquina	PPM
WENO	BSSN	$10^{-14}$	0.0141	Marquina	WENO
WENO HLLE	BSSN	$10^{-14}$	0.0141	HLLE	WENO

### III. RESULTS

#### A. Extracted gravitational waveforms

We extracted the gravitational waves at distances of 10 M, 40 M, 70 M, 100 M, and 120 M. The analysis relied on the  $l = 2$   $m = 2$  mode of the  $\psi_4$  data extracted from 100 M unless otherwise stated.

This system produced linearly polarized gravitational waves, which differ from other phenomena in gravitational wave physics which produce elliptically polarized waves. This linear polarization arises from the lack of rotation in our oscillating neutron star. In contrast, more often studied gravitational wave producing systems such as binary neutron star mergers and binary black hole mergers use their rotation to produce their gravitational waves and give their gravitational waves their elliptical polarization.

The polarization is imprinted in the real and imaginary parts of  $\psi_4$  which represent the plus and cross polarizations respectively. The real part exhibits a sinusoidal form with a frequency close to the fundamental oscillation mode frequency and on top a secular exponential decay; see Fig. 2. The imaginary part is zero to almost machine precision, indicating that no cross polarization was present.

We note that  $\psi_4$  had high frequency noise as a result of passing through refinement layers. We removed these high frequency features with low pass filters that are described in detail in the Appendix.

#### B. Convergence

We demonstrate that differences between resolutions behave as expected given the numerical method we adopt. This implies that the numerical error in our simulations can be

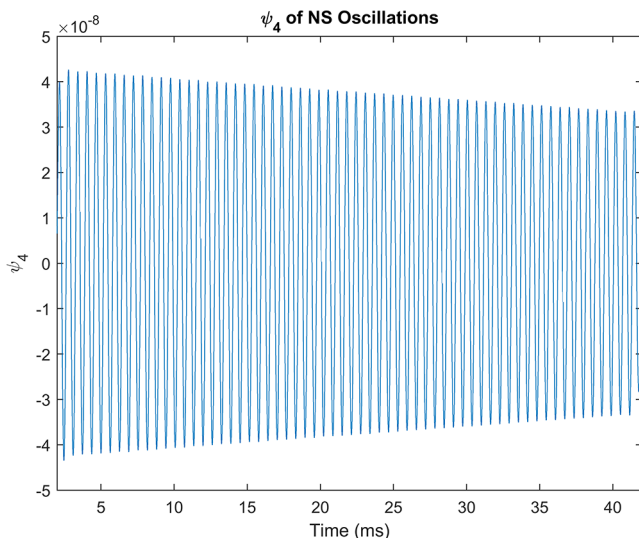


FIG. 2. The panel shows the real part of  $\psi_4$  from the PPM run with a resolution of 0.08 M. We observe that  $\psi_4$  takes the form of a decaying exponential. Furthermore, since the gravitational waves are linearly polarized, we have confirmed that the imaginary part of  $\psi_4$  vanishes.

quantified. Only with such a reliable error estimate is it possible to tell whether any damping in the gravitational waves is physically caused by gravitational radiation or by numerical dissipation. There are several possibilities to demonstrate convergence in the GW output of such models. We choose to perform convergence tests on the extrema of  $\psi_4$ .

As usual, we assume that the numerical error as represented by a Taylor expansion is dominated by the leading order term. In this case three resolutions suffice to demonstrate convergence and fit the parameters of the Taylor expansion. Specifically, the numerical solution for high, medium, and low resolutions are related by

$$\psi_{4,\text{high}} - \psi_{4,\text{med}} = c_n(\psi_{4,\text{med}} - \psi_{4,\text{low}}), \quad (13)$$

where  $c_n$  is the convergence factor of order  $n$  and is determined only by the resolutions and convergence order as

$$c_n = \frac{\Delta x_{\text{high}}^n - \Delta x_{\text{med}}^n}{\Delta x_{\text{med}}^n - \Delta x_{\text{low}}^n}. \quad (14)$$

We present the convergence order for all our numerical relativity simulations in Table II. A sample case of this analysis for the WENO reconstruction is presented in Fig. 3. Using the convergence factor and order, we were able to estimate the systematic error due to the changing resolution as

$$\text{error} = |c_n \Delta x^n|. \quad (15)$$

The results for the estimated error of the WENO reconstruction is presented in Fig. 4. This error behaves as systematic error caused by the differences in simulation resolution. As such, we did not propagate this error into the analysis because the analysis aims to characterize the effect of this same resolution dependence on the damping times.

#### C. Fourier analysis

Frequency spectra of the gravitational waveform were examined by taking the fast Fourier transform (FFT) of the  $\psi_4$  data. We plot the frequency spectrum of one of the runs in Fig. 5. We see that the most excited frequency is nearly aligned with the expected frequency of 1.579 kHz, illustrating that our perturbation excited the desired  $f$  mode. In addition, we observe at least three secondary excitations otherwise known as  $p$  modes. We have verified that the first two excitations occur at 3.710 and 5.684 kHz, which is consistent with our results.

#### D. Frequency

We also investigated the frequency evolution as the run progressed. Therefore, we took the roots of the  $\psi_4$  time series to estimate the period, which was in turn used to obtain frequency estimates for each cycle. We used the

TABLE II. Table depicting the results from our oscillating neutron star simulations. These results include the resolution of the simulation  $\Delta x$ , its frequency  $f$ , the error in that frequency  $\Delta f$ , the damping time  $\tau$ , and its estimated error  $\Delta\tau$ . The damping error is the statistical fitting error of the data and does not include any systematic errors alluded to in Secs. III B and III F. The table is divided by the simulation models described in Table I. Some cases yield convergence orders that exceed the formal accuracy of the numerical schemes involved. Such so-called overconvergence usually indicates that the data are close to but not quite within the convergent regime. At the end of each group of simulations, we include the damping time value at  $\Delta x \rightarrow 0$  using Richardson extrapolation. This procedure will systematically underestimate the error in the presence of overconvergence and should be taken with a grain of salt. We did not include errors on this value or the frequency when performing this extrapolation to infinitely fine resolution. The expected frequency and damping time for all simulations in the table according to linear theory are 1.579 kHz and 298 ms respectively.

	$\Delta x$ (M)	$f$ (kHz)	$\Delta f$ (kHz)	$\tau$ (ms)	$\Delta\tau$ (ms)	$n$
PPM big $\alpha$	0.25	1.551	0.023	45.29	0.39	4.84
	0.16	1.552	0.013	58.02	0.93	4.84
	0.125	1.555	0.017	59.81	1.65	4.84
	0.08	1.555	0.013	63.76	1.42	4.84
	0.0625	1.555	0.011	64.39	1.46	4.84
	0	...	...	64.83	...	4.84
PPM big $\rho_{\text{atm}}$	0.25	1.572	0.019	8.44	0.21	3.83
	0.16	1.579	0.014	38.36	1.56	3.83
	0.125	1.580	0.023	63.48	9.88	3.83
	0.08	1.580	0.004	178.73	3.79	3.83
	0.0625	1.581	0.004	262.11	7.58	3.83
	0	...	...	433.80	...	3.83
PPM CCZ4	0.25	1.574	0.004	8.41	0.13	3.14
	0.16	1.577	0.003	35.36	0.96	3.14
	0.125	1.579	0.004	73.21	0.57	3.14
	0.08	1.580	0.004	195.57	3.76	3.14
	0.0625	1.581	0.004	268.25	6.33	3.14
	0	...	...	376.65	...	3.14
PPM	0.25	1.573	0.005	7.47	0.16	2.98
	0.16	1.576	0.004	36.61	0.55	2.98
	0.125	1.576	0.003	73.35	1.05	2.98
	0.08	1.577	0.004	168.48	2.71	2.98
	0.0625	1.577	0.003	222.20	3.85	2.98
	0	...	...	313.74	...	2.98
WENO	0.25	1.573	0.005	80.61	0.99	2.79
	0.16	1.576	0.004	165.98	1.54	2.79
	0.125	1.577	0.004	209.60	2.14	2.79
	0.08	1.577	0.003	258.09	4.07	2.79
	0.0625	1.578	0.003	270.44	4.80	2.79
	0	...	...	283.80	...	2.79
WENO HLLE	0.25	1.574	0.005	124.48	8.42	5.77
	0.16	1.576	0.004	195.72	1.71	5.77
	0.125	1.577	0.003	232.12	2.44	5.77
	0.08	1.579	0.011	265.56	2.80	5.77
	0.0625	1.578	0.003	275.47	5.00	5.77
	0	...	...	290.37	...	5.77

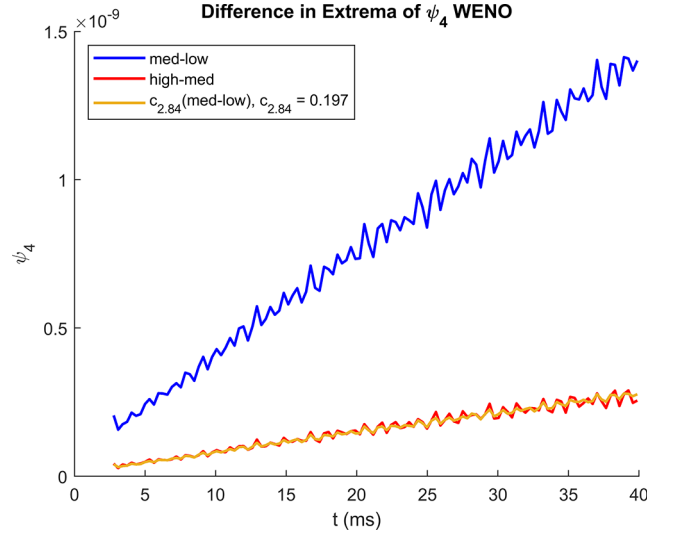


FIG. 3. Convergence of the extrema of  $\psi_4$ . Here low, med, high refer to runs with fine resolutions of 0.125 M, 0.08 M, and 0.0625 M respectively for the WENO case. This information can be inferred by noticing that the resolutions satisfy the relation  $(\text{high} - \text{med}) = c_n(\text{med} - \text{low})$ ; see Eq. (13). We found  $c_n \sim 0.197$  by taking  $c_n$  to be the best fit of our data to Eq. (13). Using Eq. (14) for  $c_{2.84} \sim 0.197$ , we found that  $n = 2.84$  which is consistent with the assumed order of convergence. This result is close to the order of our lowest order contributions to our numerical method, which demonstrates both the convergence and internal consistency of our numerical methods. We acknowledge that the value in this plot differs from that quoted in Table II as this convergence test applies to a longer portion of the waveform. The value quoted in Table II only uses the portion of the waveform that was used to compute the damping times. See Sec. III F for more details.

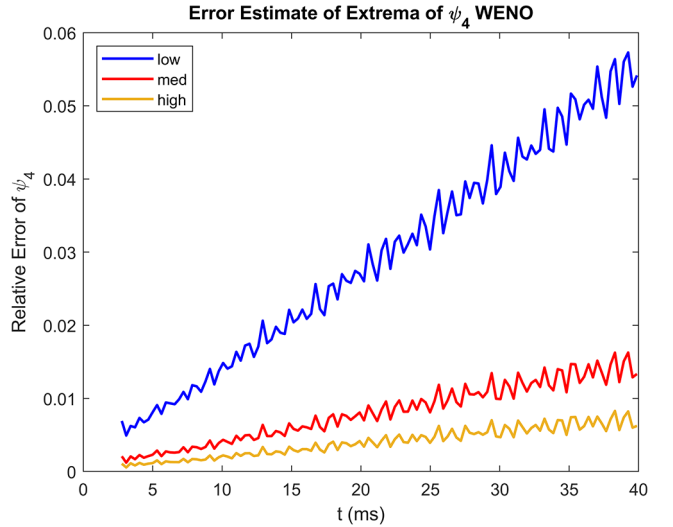


FIG. 4. Estimate for the relative error in  $\psi_4$ . Here low, med, high refer to runs with fine resolutions of 0.125 M, 0.08 M, and 0.0625 M respectively for the WENO case. This error estimate was obtained using Eq. (15) and dividing by the value of  $\psi_4$  at each instant in time. Unlike Fig. 3 where we used a constant value of  $c_n$  for a best fit to Eq. (13), our value of  $c_n$  and  $n$  here are solutions to Eqs. (13) and (14) at each point in time.

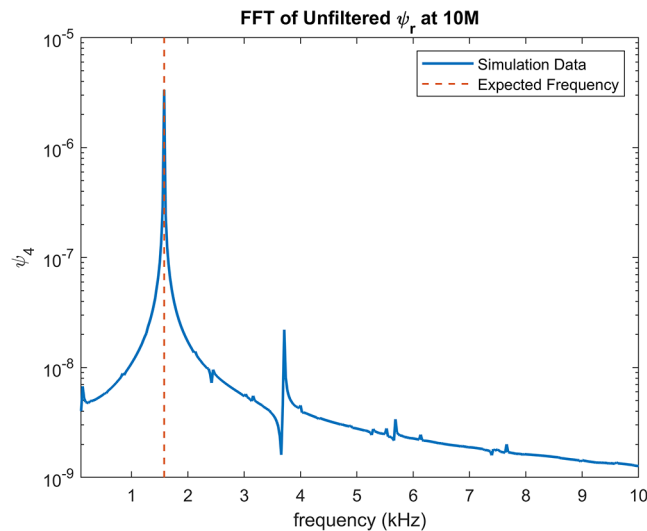


FIG. 5. Fast Fourier transform (FFT) of the  $\psi_4$  data from WENO HLL simulation with a fine resolution of 0.0625 M. The gravitational waves here were extracted from 10 M. The 10M data best illuminate the excitations in the frequency spectrum because it occurs before any AMR boundary introduces high frequency features (we also present the frequency spectrum extracted at 100 M in Fig. 10). We note the primary is near the expected  $f$ -mode excitation frequency of 1.579 kHz. We also observe secondary excitations at 3.710, 5.684, and 7.658 kHz which are consistent with the first overtones ( $p$  modes) of the  $f$  mode. We note that the spikes at the higher frequencies are suppressed after applying the filtering. See the Appendix for more details.

average frequency as the value for the simulation and the standard deviation as the error.

Although most of the runs exhibited constant frequency regardless of resolution, runs with high-density atmospheres of  $10^{-10} \text{ M}^{-2}$  and a length longer than 10 ms experienced a rise in frequency as the runs progressed.

In contrast, the frequency of the low-density atmosphere runs of  $10^{-14} \text{ M}^{-2}$  remained constant for even the longest runs which lasted 50 ms. We can see the frequency evolution in Fig. 6. The likely physical cause of this behavior is accretion of artificial atmosphere material onto the star which leads to a steady change in the background stellar model and hence a slight change in its fundamental oscillation frequencies.

We found that the frequency was fairly independent of resolution as displayed in Table II, though the higher amplitude runs did experience a lower frequency than the lower perturbation runs. The frequencies all appear to be around 1.579 kHz which is the expected frequency for  $f$ -mode oscillations based on linear theory.

We note that since the gravitational waves were linearly polarized, we could not determine instantaneous frequency by taking the derivative of the phase of the gravitational waves as the imaginary part was nearly zero.

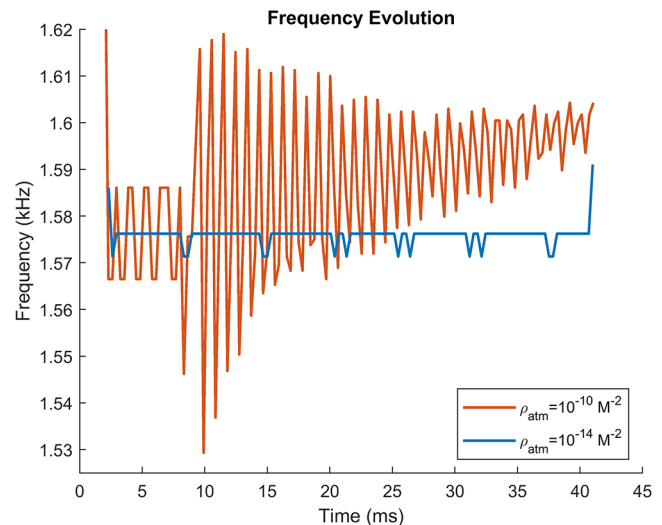


FIG. 6. Frequency evolution of the waveform as time progressed of the PPM and PPM big  $\rho_{\text{atm}}$  runs at a fine resolution of 0.125 M. This frequency was computed by examining the roots of the waveform time series and finding the time interval between them. This allows us to track the frequency evolution throughout the run. For the high atmosphere plot in red, the frequency increases after about 10 ms. The low atmosphere run in blue remained constant throughout the entirety of the run.

### E. Damping times

Damping times were extracted by performing linear fits to the natural log of the extrema of  $\psi_4$ , as shown in Fig. 7. Error estimates were computed using the standard deviations of the damping time calculations using the extrema of

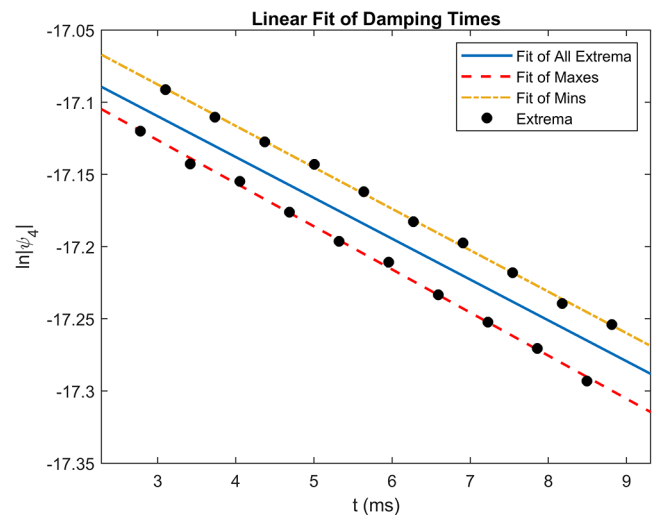


FIG. 7. Linear fit of the extrema of  $\psi_4$  that was used to obtain damping times of the gravitational waves for the PPM CCZ4 simulation with a fine resolution of 0.16 M. We note in particular that the extrema of  $\psi_4$  differed by an offset that may skew the results. Therefore, we examined the slopes computed using the maxima and minima individually to provide an error estimate for the damping time of each simulation. The quoted value for the damping times was computed using the full dataset of extrema.

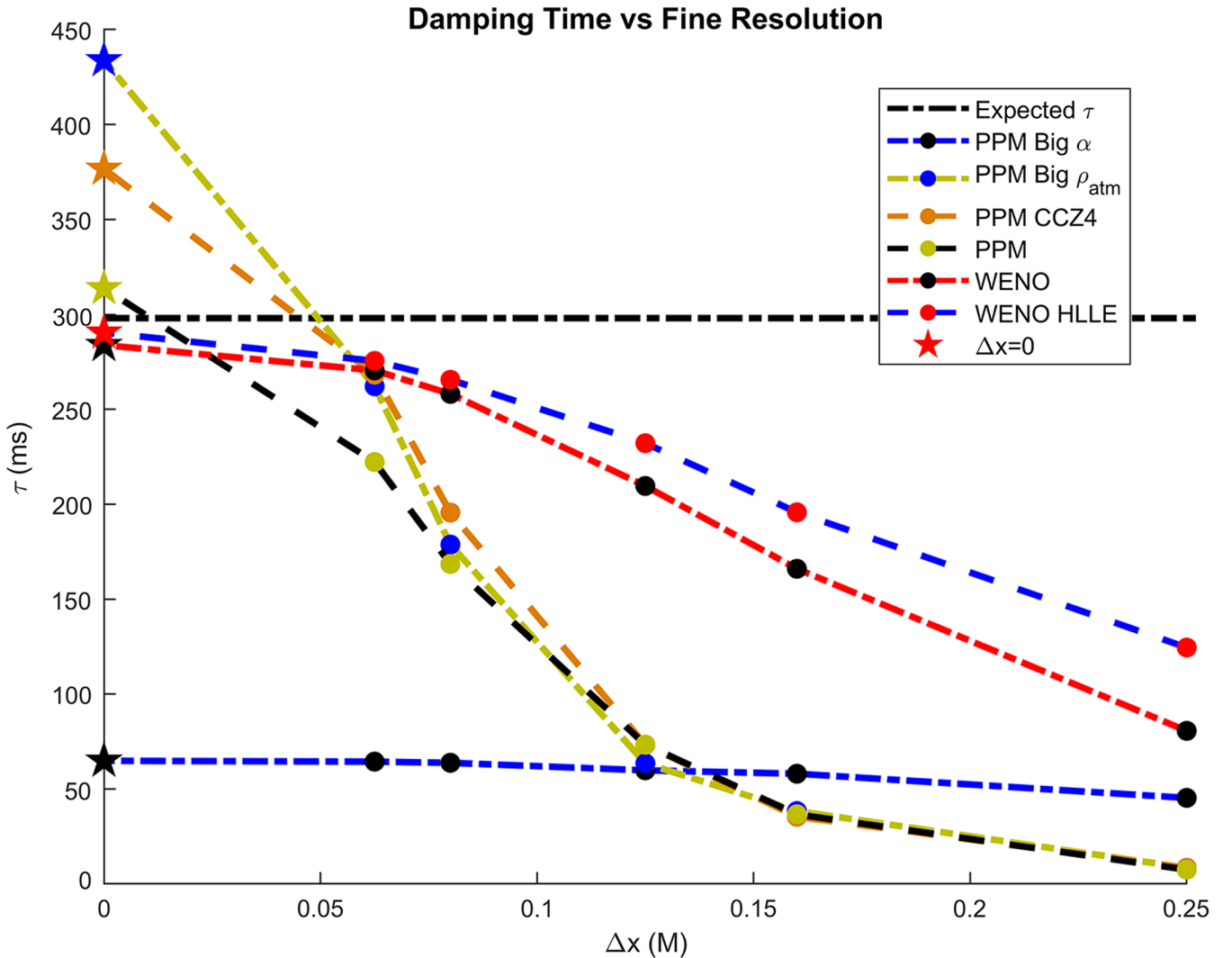


FIG. 8. Damping times for simulations of neutron star  $f$ -mode oscillations as a function of fine resolution. The black dash-dot line represents the expected damping time for a static TOV of this mass computed using linear theory. The star value at  $\Delta x \rightarrow 0$  M is the value obtain for the frequencies by extrapolating to infinite resolution. We notice that the runs using PPM reconstruction behaved similarly to one another. However, the high atmosphere PPM  $\rho_{\text{atm}}$  and PPM CCZ4 runs diverge from the PPM run at finer resolutions. This causes the Richardson extrapolated value of those high atmosphere sequences to significantly overshoot the expected damping time from linear theory. We described in Sec. III D that the high atmosphere runs experienced increased frequency as the run progressed. We believe the effects of this evolving frequency propagate into the damping time calculation, leading to the divergence of these sequences of damping times. The WENO reconstruction runs also exhibited similar characteristics. In addition, the WENO runs are significantly more accurate than the PPM runs at a given resolution. PPM models required twice the resolution than the WENO models for similar accuracy. The high perturbation run exhibited entirely different damping time characteristics from the others, indicating that it was likely not in the linear perturbation regime.

$\psi_4$  individually rather than from all the extrema in the simulation dataset.

To compute the damping times from our suite of numerical relativity simulations we used the WENO and PPM reconstruction methods, finding that the former is much more robust and accurate than the latter. We also show results for a sample simulation, “PPM big  $\alpha$ ” in Fig. 8, whose perturbation amplitude is 10 times larger than those that reproduce predictions in the linear regime. This

simulation was prepared to exhibit the nonlinear regime of neutron star  $f$ -mode oscillations. Since simulations with  $\Delta x < 0.0625$  M were deemed to be too computationally intensive to run, we extrapolated these results to the continuum limit to see if they approach the expected value of 298 ms. We used Richardson extrapolation with unequal resolution ratios to estimate the value at infinitely fine resolution. A summary of these calculations is presented in Table II.

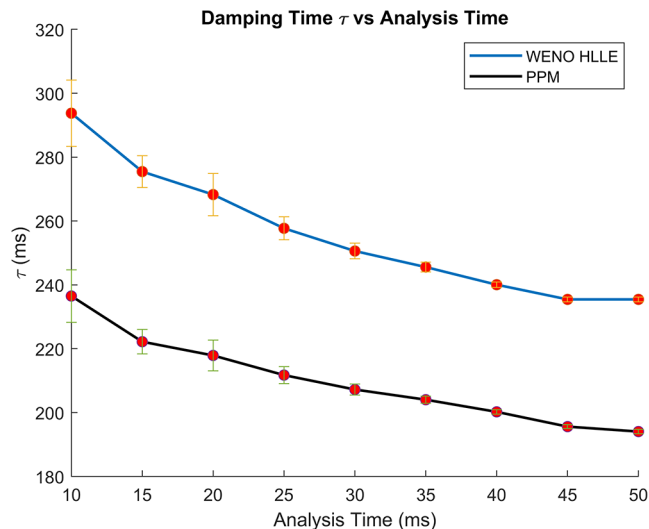


FIG. 9. Plot of the damping time  $\tau$  vs analysis time with the statistical fitting error at each data point for the WENO HLLE and PPM datasets with  $\Delta x = 0.0625 M$ . The analysis time is defined as the cutoff time for waveform data to be used in the analysis. Data beyond the analysis time were discarded for the purpose of the analysis. The first 2 ms of data which are included in the analysis were also discarded to allow for any transient effects to decay. We notice that statistical error clearly decreases as the analysis time increases. However, we observe that  $\tau$  decreases away from the expected value of 298 ms with increased analysis time. We noticed that in both curves in the plot there appears to be a local minimum in the statistical uncertainty at an analysis time of 15. As such, we selected an analysis time of 15 ms for the damping time analysis in this paper.

Figure 8 shows that the WENO reconstruction approaches the linear perturbation prediction of 298 ms for the highest-resolution run of each simulation. The three simulations that significantly depart from the linear perturbation regime correspond to two categories: (i) The two simulations with damping times much larger than 298 ms correspond to simulations with large artificial atmospheres,  $\rho_{\text{atm}} \sim 10^{-10} M^{-2}$ ; (ii) the simulation with estimated damping time much smaller than 298 ms is clearly outside of the linear perturbation regime by construction.

These results indicate that provided a numerical setup in which the atmosphere used for the simulations satisfies  $\rho_{\text{atm}} \lesssim 10^{-14} M^{-2}$  and the perturbation applied to the TOV star is within the linear regime, the extracted damping times with the WENO reconstruction method from our suite of numerical simulations is consistent with linear perturbation predictions.

### F. Evolution of damping time

High-resolution runs with longer damping times required longer analysis times to obtain satisfactory statistical fits. This necessity derives from the difference in position of individual points being significant compared to the

difference induced by the true damping of the waveform over short timescales. In essence, the longer we run the simulation, the closer we get to running for the damping time we would like to measure; thereby, we reduce the statistical fitting error in the damping time.

Although increasing the run time decreases the statistical error in the damping time, it introduces systematic error in the damping time calculation. We found that as the run progressed, the waveform did not exhibit a true exponential decay. Instead, the waveform systematically decayed quicker than an exponential damping time would suggest at long times. This posits the existence of some other source of decay in the waveforms, most likely some form of numerical dissipation.

Figure 9 illustrates the evolution of the damping time value vs the analysis time, the cutoff time for waveform data in the analysis to calculate the damping time beyond which the data would not be used for such an analysis. We also note that the first 2 ms of data also were not used in the analysis to allow time for any transients to die out. In addition, the figure depicts the statistical fitting error at each of those points. One can observe that the damping time and statistical error decrease as the analysis time increases. We observed a local minimum in the statistical error at an analysis time of 15 ms and thus chose that analysis time for the computation of the damping times in Table II.

## IV. CONCLUSIONS

We have carried out systematic analyses of the accuracy needed to extract the frequency and damping time of  $f$ -mode oscillations. We have demonstrated the robustness of our results by extracting these observables, and demonstrating that our results are similar when using both the WENO and PPM reconstruction methods.

We have shown that for small perturbations, the damping times extracted from our numerical relativity simulations are consistent with linear theory perturbations when we consider atmospheres  $\rho_{\text{atm}} \leq 10^{-14} M^{-2}$ . On the other hand, we have found that if artificial atmospheres are poorly chosen,  $\rho_{\text{atm}} \leq 10^{-10} M^{-2}$ , the extracted damping times from our numerical simulations differ significantly from linear perturbation predictions at evolutions  $\gtrsim 10$  ms. This may be caused due to accretion of the atmosphere, which introduces a secular change (increased mass) in the background solution.

The convergence analyses we have presented suggest that even for a careful choice of numerical schemes a minimum resolution of  $\sim 0.125 M$  is needed to accurately extract the GW induced damping time of  $f$ -mode oscillations. WENO reconstruction clearly outperforms the PPM scheme, which needed twice the resolution to obtain similar accuracies in the damping times. This resolution is within the range of existing neutron star numerical relativity simulations that have been presented in the literature albeit on the more computationally expensive end.

Having established a blueprint of numerical accuracy to extract the frequency and damping times of  $f$  modes, in future work we will put this setup to use and investigate the accuracy with which we can infer properties of the EOS through GW observations of highly eccentric neutron star encounters.

### ACKNOWLEDGMENTS

This research is part of the Blue Waters sustained-petascale computing project, which is supported by the National Science Foundation (Grants No. OCI-0725070 and No. ACI-1238993) and the State of Illinois. Blue Waters is a joint effort of the University of Illinois at Urbana-Champaign and its National Centre for Supercomputing Applications.

Some numerical results were obtained using the University of Maryland Deepthought2 HPC Cluster. This work was supported in part by joint research workshop Grant No. 2015/50421-8 from FAPESP and the University of Maryland, College Park. This work was supported in part by Perimeter Institute for Theoretical Physics. Research at Perimeter Institute is supported by the Government of Canada through the Department of Innovation, Science and Economic Development Canada and by the Province of Ontario through the Ministry of Research, Innovation and Science. We acknowledge support from the NCSA. Grants No. NSF-1550514 and No. NSF-1659702 are gratefully acknowledged. We thank the NCSA Gravity Group for useful feedback.

### APPENDIX: FILTERING

Initially, the  $\psi_4$  data contained significant high frequency noise that interfered with our analysis. We noted that the signals extracted from 10 M, before passing through the first refinement boundary, did not exhibit any such high frequency noise. Therefore, we hypothesized that it passed through the various refinement boundaries as it traveled to the relevant extraction sphere at 100 M.

To compensate for this high frequency behavior induced from the refinement layers, we applied a low pass filter to the raw data. Specifically, we applied a butter filter with zero phase filtering. Relative to the sample frequency, the filter had a passband frequency of 0.01 and a stop band frequency of 0.04. The passband ripple amplitude of the filter was 1 dB and the stop band attenuation was 60 dB. This filtering was essential to ensuring the extracted  $\psi_4$  produced meaningful data analysis especially for the damping times. Figures 10 and 11 illustrate the effect of the filtering on the data. We observe the frequency spectrum before and after the filtering by looking at the FFTs extracted at 100 M in Fig. 12. We observe that the unfiltered frequency spectrum is very noisy, which is most apparent after the second peak. The filtering eliminates this noise. However, the filtering also significantly suppresses the second peak and renders the third and fourth invisible.

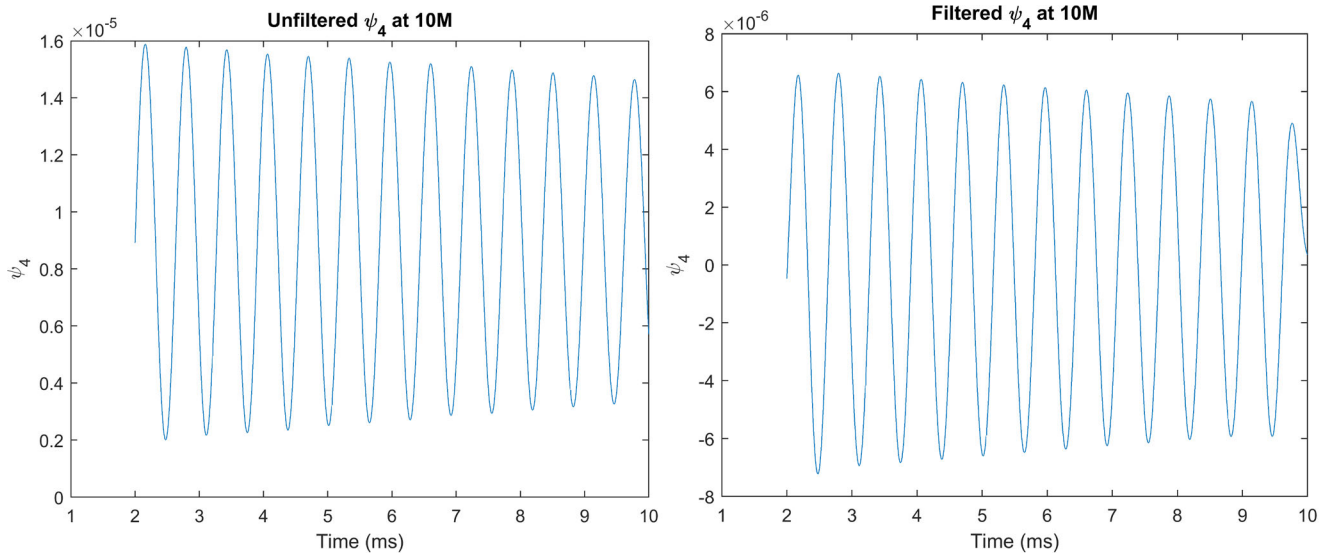


FIG. 10. Plot of the  $\psi_4$  data extracted at 10 M. The left plot depicts the unfiltered data. We note that the unfiltered data lack any sort of high frequency component as they have yet to pass through a refinement boundary. When we filter the data as in the right plot, we observe that the waveform is now centered at the origin rather than offset as it had been previously. The waveform is also hardly distorted, with most of the distortion occurring at the end of the waveform.

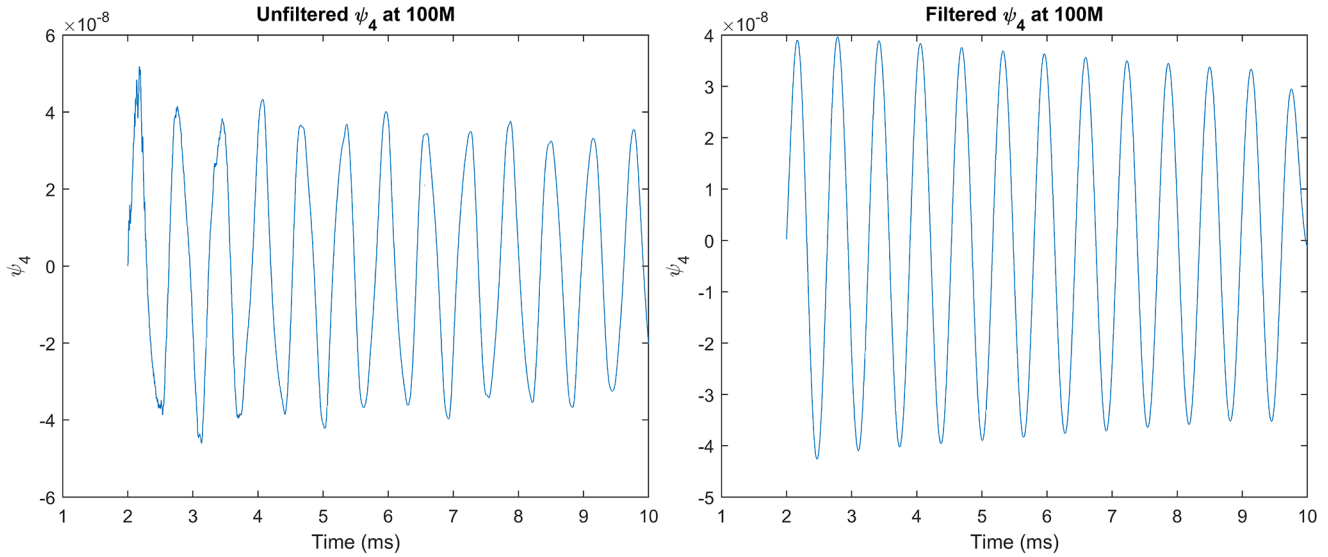


FIG. 11. Plot of the  $\psi_4$  data extracted at 100 M. The left plot depicts the unfiltered data. We note that the unfiltered data are much noisier than the data extracted at 10 M in Fig. 10, having passed through multiple refinement layers. These refinement layers are believed to induce high frequency noise in the waveform. In the plot, we show the postfiltered data. Compared to Fig. 10 the data have been significantly changed by the filtering. In turn, the postfiltered data appear to match the data in Fig. 10 much more closely. This supports the notion that the unfiltered 100 M data were contaminated by high frequency noise passing through refinement boundaries. We also note that the end of the waveform is distorted in a similar manner as Fig. 10. For this reason, we removed the end of the data from the computation of the damping times.

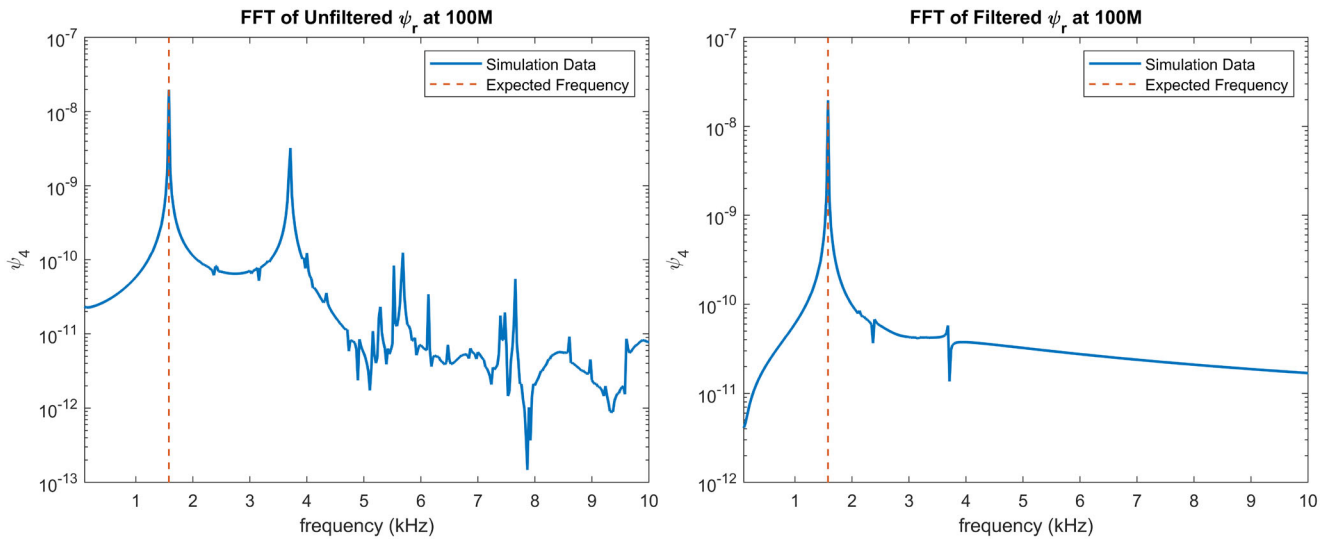


FIG. 12. Plots of the FFTs of the WENO HLLC simulation with a fine resolution of 0.0625 M before and after the filtering. The gravitational waves here were extracted from 100 M, the portion that was analyzed to extract the frequencies and damping times. The left plot illustrates the unfiltered FFT, which contains the four distinct peaks seen in Fig. 5. However, there is a significant amount of noise after the second peak. On the right we show the FFT after the filtering has been applied. We observed that the noise is no longer present. However, the second peak is significantly suppressed, while the third and fourth peaks are no longer visible. Thus we did not consider effects from these modes in our analysis of the frequency or damping times.

- [1] L. Landau, *Phys. Z. Sowjetunion* **1**, 285 (1932).
- [2] J. R. Stone, *Eur. Phys. J. A* **52**, 66 (2016).
- [3] C. Alcock, E. Farhi, and A. Olinto, *Astrophys. J.* **310**, 261 (1986).
- [4] D. G. Yakovlev and C. J. Pethick, *Annu. Rev. Astron. Astrophys.* **42**, 169 (2004).
- [5] F. Weber, *Prog. Part. Nucl. Phys.* **54**, 193 (2005).
- [6] B. P. Abbott, R. Abbott, T. D. Abbott, F. Acernese, K. Ackley, C. Adams, T. Adams, P. Addesso, R. X. Adhikari, V. B. Adya *et al.*, *Phys. Rev. Lett.* **119**, 161101 (2017).
- [7] B. P. Abbott, R. Abbott, T. D. Abbott, F. Acernese, K. Ackley, C. Adams, T. Adams, P. Addesso, R. X. Adhikari, V. B. Adya *et al.*, *Astrophys. J. Lett.* **848**, L12 (2017).
- [8] E. Fonseca, T. T. Pennucci, J. A. Ellis, I. H. Stairs, D. J. Nice, S. M. Ransom, P. B. Demorest, Z. Arzoumanian, K. Crowter, T. Dolch, R. D. Ferdman, M. E. Gonzalez, G. Jones, M. L. Jones, M. T. Lam, L. Levin, M. A. McLaughlin, K. Stovall, J. K. Swiggum, and W. Zhu, *Astrophys. J.* **832**, 167 (2016).
- [9] J. Antoniadis *et al.*, *Science* **340**, 1233232 (2013).
- [10] L. Rezzolla, E. R. Most, and L. R. Weih, *Astrophys. J. Lett.* **852**, L25 (2018).
- [11] B. Margalit and B. D. Metzger, *Astrophys. J. Lett.* **850**, L19 (2017).
- [12] A. Bauswein, T. W. Baumgarte, and H.-T. Janka, *Phys. Rev. Lett.* **111**, 131101 (2013).
- [13] C. L. Fryer, K. Belczynski, E. Ramirez-Ruiz, S. Rosswog, G. Shen, and A. W. Steiner, *Astrophys. J.* **812**, 24 (2015).
- [14] S. Lawrence, J. G. Tervala, P. F. Bedaque, and M. C. Miller, *Astrophys. J.* **808**, 186 (2015).
- [15] K. C. Gendreau, Z. Arzoumanian, and T. Okajima, *Proc. SPIE Int. Soc. Opt. Eng.* **8443**, 844313 (2012).
- [16] S. N. Zhang *et al.*, *Proc. SPIE* **9905**, 99051Q (2017).
- [17] D. Psaltis, F. Özel, and D. Chakrabarty, *Astrophys. J.* **787**, 136 (2014).
- [18] M. C. Miller, [arXiv:1312.0029](https://arxiv.org/abs/1312.0029).
- [19] M. C. Miller and F. K. Lamb, *Eur. Phys. J. A* **52**, 63 (2016).
- [20] B. P. Abbott, R. Abbott, T. D. Abbott, M. R. Abernathy, F. Acernese, K. Ackley, C. Adams, T. Adams, P. Addesso, R. X. Adhikari *et al.*, *Phys. Rev. Lett.* **116**, 131103 (2016).
- [21] J. Aasi *et al.* (LIGO Scientific Collaboration), *Classical Quantum Gravity* **32**, 115012 (2015).
- [22] F. Acernese *et al.*, *Classical Quantum Gravity* **32**, 024001 (2015).
- [23] D. A. Coulter, R. J. Foley, C. D. Kilpatrick, M. R. Drout, A. L. Piro, B. J. Shappee, M. R. Siebert, J. D. Simon, N. Ulloa, D. Kasen, B. F. Madore, A. Murguía-Berthier, Y.-C. Pan, J. X. Prochaska, E. Ramirez-Ruiz, A. Rest, and C. Rojas-Bravo, *Science* **358**, 1556 (2017).
- [24] L. Lindblom, *Phys. Rev. D* **82**, 103011 (2010).
- [25] L. Lindblom and N. M. Indik, *Phys. Rev. D* **86**, 084003 (2012).
- [26] F. Douchin and P. Haensel, *Astron. Astrophys.* **380**, 151 (2001).
- [27] B. P. Abbott *et al.* (LIGO Scientific and Virgo Collaborations), *Phys. Rev. Lett.* **121**, 161101 (2018).
- [28] L. Blanchet, *Living Rev. Relativity* **9**, 4 (2006).
- [29] S. Rosswog, E. Ramirez-Ruiz, and M. B. Davies, *Mon. Not. R. Astron. Soc.* **345**, 1077 (2003).
- [30] R. Haas, C. D. Ott, B. Szilagyi, J. D. Kaplan, J. Lippuner, M. A. Scheel, K. Barkett, C. D. Muhlberger, T. Dietrich, M. D. Duez, F. Foucart, H. P. Pfeiffer, L. E. Kidder, and S. A. Teukolsky, *Phys. Rev. D* **93**, 124062 (2016).
- [31] A. Parisi and R. Sturani, *Phys. Rev. D* **97**, 043015 (2018).
- [32] R. F. P. Mendes and N. Ortiz, *Phys. Rev. Lett.* **120**, 201104 (2018).
- [33] R. Gold, S. Bernuzzi, M. Thierfelder, B. Brügmann, and F. Pretorius, *Phys. Rev. D* **86**, 121501 (2012).
- [34] W. E. East, F. Pretorius, and B. C. Stephens, *Phys. Rev. D* **85**, 124009 (2012).
- [35] W. E. East and F. Pretorius, *Astrophys. J.* **760**, L4 (2012).
- [36] W. E. East, V. Paschalidis, and F. Pretorius, *Classical Quantum Gravity* **33**, 244004 (2016).
- [37] W. E. East, V. Paschalidis, F. Pretorius, and S. L. Shapiro, *Phys. Rev. D* **93**, 024011 (2016).
- [38] L. J. Papenfort, R. Gold, and L. Rezzolla, *Phys. Rev. D* **98**, 104028 (2018).
- [39] S. V. Chaurasia, T. Dietrich, N. K. Johnson-McDaniel, M. Ujevic, W. Tichy, and B. Brügmann, *Phys. Rev. D* **98**, 104005 (2018).
- [40] C. Chirenti, R. Gold, and M. C. Miller, *Astrophys. J.* **837**, 67 (2017).
- [41] E. A. Huerta, P. Kumar, B. Agarwal, D. George, H.-Y. Schive, H. P. Pfeiffer, R. Haas, W. Ren, T. Chu, M. Boyle, D. A. Hemberger, L. E. Kidder, M. A. Scheel, and B. Szilagyi, *Phys. Rev. D* **95**, 024038 (2017).
- [42] E. A. Huerta, P. Kumar, S. T. McWilliams, R. O’Shaughnessy, and N. Yunes, *Phys. Rev. D* **90**, 084016 (2014).
- [43] E. A. Huerta and D. A. Brown, *Phys. Rev. D* **87**, 127501 (2013).
- [44] E. A. Huerta, C. J. Moore, P. Kumar, D. George, A. J. K. Chua, R. Haas, E. Wessel, D. Johnson, D. Glennon, A. Rebei, A. M. Holgado, J. R. Gair, and H. P. Pfeiffer, *Phys. Rev. D* **97**, 024031 (2018).
- [45] A. Rebei, E. A. Huerta, S. Wang, S. Habib, R. Haas, D. Johnson, and D. George, [arXiv:1807.09787](https://arxiv.org/abs/1807.09787).
- [46] A. Bauswein, N. Stergioulas, and H.-T. Janka, *Phys. Rev. D* **90**, 023002 (2014).
- [47] K. Takami, L. Rezzolla, and L. Baiotti, *Phys. Rev. Lett.* **113**, 091104 (2014).
- [48] S. M. Morsink, N. Stergioulas, and S. R. Blattnig, *Astrophys. J.* **510**, 854 (1999).
- [49] B. Zink, O. Korobkin, E. Schnetter, and N. Stergioulas, *Phys. Rev. D* **81**, 084055 (2010).
- [50] J. Steinhoff, T. Hinderer, A. Buonanno, and A. Taracchini, *Phys. Rev. D* **94**, 104028 (2016).
- [51] H. Yang, W. E. East, V. Paschalidis, F. Pretorius, and R. F. P. Mendes, *Phys. Rev. D* **98**, 044007 (2018).
- [52] N. Andersson and K. D. Kokkotas, *Mon. Not. R. Astron. Soc.* **299**, 1059 (1998).
- [53] O. Benhar, V. Ferrari, and L. Gualtieri, *Phys. Rev. D* **70**, 124015 (2004).
- [54] G. Lioutas and N. Stergioulas, *Gen. Relativ. Gravit.* **50**, 12 (2018).
- [55] L. K. Tsui and P. T. Leung, *Mon. Not. R. Astron. Soc.* **357**, 1029 (2005).
- [56] H. K. Lau, P. T. Leung, and L. M. Lin, *Astrophys. J.* **714**, 1234 (2010).

- [57] C. Chirenti, G. H. de Souza, and W. Kastaun, *Phys. Rev. D* **91**, 044034 (2015).
- [58] É. É. Flanagan and T. Hinderer, *Phys. Rev. D* **77**, 021502 (2008).
- [59] K. Yagi and N. Yunes, *Science* **341**, 365 (2013).
- [60] K. Yagi and N. Yunes, *Phys. Rev. D* **88**, 023009 (2013).
- [61] K. Yagi and N. Yunes, *Phys. Rev. D* **89**, 021303 (2014).
- [62] L. Baiotti, S. Bernuzzi, G. Corvino, R. De Pietri, and A. Nagar, *Phys. Rev. D* **79**, 024002 (2009).
- [63] T. Dietrich, S. Bernuzzi, B. Bruegmann, and W. Tichy, [arXiv:1803.07965](https://arxiv.org/abs/1803.07965).
- [64] L. Gondán and B. Kocsis, *Astrophys. J.* **871**, 178 (2019).
- [65] M. Alcubierre, *Introduction to 3+1 Numerical Relativity* (Oxford University Press, Oxford, 2008).
- [66] C. Bona, C. Palenzuela-Luque, and C. Bona-Casas, *Elements of Numerical Relativity and Relativistic Hydrodynamics: From Einstein's Equations to Astrophysical Simulations*, Lecture Notes in Physics (Springer, Berlin, 2009).
- [67] T. W. Baumgarte and S. L. Shapiro, *Numerical Relativity: Solving Einstein's Equations on the Computer* (Cambridge University Press, Cambridge, England, 2010).
- [68] E.ourgoulhon, *Lecture Notes in Physics* (Springer Verlag, Berlin, 2012), Vol. 846.
- [69] L. Rezzolla and O. Zanotti, *Relativistic Hydrodynamics* (Oxford University Press, Oxford, 2013).
- [70] M. Shibata, *Numerical Relativity* (World Scientific, Singapore, 2016).
- [71] M. Shibata and T. Nakamura, *Phys. Rev. D* **52**, 5428 (1995).
- [72] T. W. Baumgarte and S. L. Shapiro, *Phys. Rev. D* **59**, 024007 (1998).
- [73] D. Alic, C. Bona-Casas, C. Bona, L. Rezzolla, and C. Palenzuela, *Phys. Rev. D* **85**, 064040 (2012).
- [74] L. Baiotti and L. Rezzolla, *Rep. Prog. Phys.* **80**, 096901 (2017).
- [75] D. Brown, P. Diener, O. Sarbach, E. Schnetter, and M. Tiglio, *Phys. Rev. D* **79**, 044023 (2009).
- [76] F. Löffler, J. Faber, E. Bentivegna, T. Bode, P. Diener, R. Haas, I. Hinder, B. C. Mundim, C. D. Ott, E. Schnetter, G. Allen, M. Campanelli, and P. Laguna, *Classical Quantum Gravity* **29**, 115001 (2012).
- [77] H. O. Kreiss and J. Olinger, *Methods for the Approximate Solution of Time Dependent Problems* (GARP Publication Series, Geneva, 1973), Vol. 10.
- [78] F. Banyuls, J. A. Font, J. M. Ibáñez, J. M. Martí, and J. A. Miralles, *Astrophys. J.* **476**, 221 (1997).
- [79] P. Mösta, B. C. Mundim, J. A. Faber, R. Haas, S. C. Noble, T. Bode, F. Löffler, C. D. Ott, C. Reisswig, and E. Schnetter, *Classical Quantum Gravity* **31**, 015005 (2014).
- [80] D. I. Jones, N. Andersson, and N. Stergioulas, *Mon. Not. R. Astron. Soc.* **334**, 933 (2002).
- [81] E. Schnetter, S. H. Hawley, and I. Hawke, *Classical Quantum Gravity* **21**, 1465 (2004).
- [82] T. Goodale, G. Allen, G. Lanfermann, J. Massó, T. Radke, E. Seidel, and J. Shalf, in *Proceedings of the 5th International Conference, Vector and Parallel Processing-VECPAR'2002*, Lecture Notes in Computer Science (Springer, Berlin, 2003).
- [83] E. T. Newman and R. Penrose, *J. Math. Phys. (N.Y.)* **3**, 566 (1962); **4**, 998(E) (1963).
- [84] N. T. Bishop and L. Rezzolla, *Living Rev. Relativity* **19**, 2 (2016).
- [85] J. N. Goldberg, A. J. MacFarlane, E. T. Newman, F. Rohrlich, and E. C. G. Sudarshan, *J. Math. Phys. (N.Y.)* **8**, 2155 (1967).